Studies in JET Divertors of Varied Geometry II: Impurity Seeded Plasmas

G F Matthews, B Balet, J G Cordey, S J Davies, G Fishpool, H-Y Guo, L D Horton, M von Hellermann, L C Ingesson, J Lingertat, A Loarte[1], G M McCracken, C F Maggi, R D Monk, V Parail, R Reichle[2], M F Stamp, P C Stangeby[3], D Stork, A Taroni, G Vlases, K-D Zastrow.

JET Joint Undertaking, Abingdon, Oxfordshire, OX14 3EA,
[1] Present Address: The NET Team, Max-Planck Institut für Plasmaphysic, D-85748 Garching, Germany.
[2] Present Address: Département de Recherches sur la Fusion Contrõlée, Association Euratom-CEA, Centre d'Etudes de Cadarache, F-13108 Saint-Paul-lez-Durance, France.
[3] and Institute for Aerospace Studies, University of Toronto, Canada.

ABSTRACT

In current large tokamaks non-intrinsic seeded impurities have been used to produce divertor power loads which would be considered acceptable when extrapolated to ITER. Many devices have achieved the goal of high fractional radiated powers, small frequent ELMs and detachment which are characteristic of radiative H-mode regimes. However, it has been a matter of concern that the Z_{eff} associated with the seeded impurities may exceed that allowable in ITER and also that the degradation in energy confinement may be unacceptable. Confidence can only be built in the prediction of these parameters in ITER if reliable scalings are available for impurity content and energy confinement which have a sound physics basis. This paper describes work at JET in this area whilst using multi-machine data to characterise the size scaling and provide a context for the JET data. Predicted levels for the impurity content of seeded ITER plasmas appear to be of marginal acceptability. The situation with regard to confinement is less clear. Dimensionless parameter scaling experiments have been conducted in which β, q_{95}, fractional radiated power and Z_{eff} are held constant for a range of ρ_*. The scaling of global energy confinement derived from these radiative discharges appears to be Bohm-like. However, local transport analysis of JET pulses using the TRANSP code suggests that the effective thermal diffusivity of the core retains its gyro-Bohm like scaling.

1. INTRODUCTION

Radiative plasmas which are partially detached from the divertor target plates are considered by the ITER design team to be the preferred solution to the problems of reducing the peak power and erosion of divertor components to acceptable levels [*Janeschitz*]. In current limiter and divertor experiments, non-intrinsic impurities have been used to increase the radiated power fraction to levels considered appropriate for *ITER* [*Allen, Itami, Lipschultz, Matthews95b, Neuhauser, Samm*] and have achieved partial or complete detachment [*Matthews95a*]. The most critical parameters for the ITER operating point are indicated in table 1 [*Janeschitz, Putvinski*]:

The JET Mark IIA divertor was installed in 1996. Since that time experiments have been performed to characterise the performance of this more closed geometry as compared with its predecessor the Mark I divertor [*Horton, Stork, Vlases96*], as shown in figure 1.0.1. The Mark IIA divertor has been operated both with significant leakage paths for neutrals from the divertor pumping plenum to the main chamber and with these leaks reduced by a factor of three("plugged": Mark IIAP) [*Altmann*]. There has thus been a progression from the original very shallow and open JET divertor configuration (Mark 0) which was used until 1992 [*Vlases*], to the deeper but still very open Mark I, and then to the more closed and ITER relevant Mark IIA and Mark IIAP. In this paper we concentrate on plasmas with impurities deliberately added ("seeding") to increase the radiated power. A companion paper [*Horton*] discusses operation without seeding,

while a third paper in this series explores the behaviour of intrinsic impurities in the various JET divertor geometries [*McCracken98*].

| Parameter	ITER requirement
P_{sep}/P_{H-L}	>1
$H_{ITERL89-P(\sim Bohm)}$	2.6 ignition (>1.8 driven)
$H_{ITERH93-P(\sim Gyro-Bohm)}$	0.85 ignition(>0.68 driven)
β_N	2.25
q_{95}	3.1
$n_e/n_{G(Greenwald\ Limit)}$	1.1
Z_{eff}	<1.8 (1.6 excluding He)
$f_{rad} = P_{rad}/(P_{heat}-P_{brems})$	75%
Target material	C (W tiles on baffle)
Divertor regime	Partially detached (with small ELMs)
Divertor geometry	Closed/ vertical target

Table 1: Key ITER reference parameters
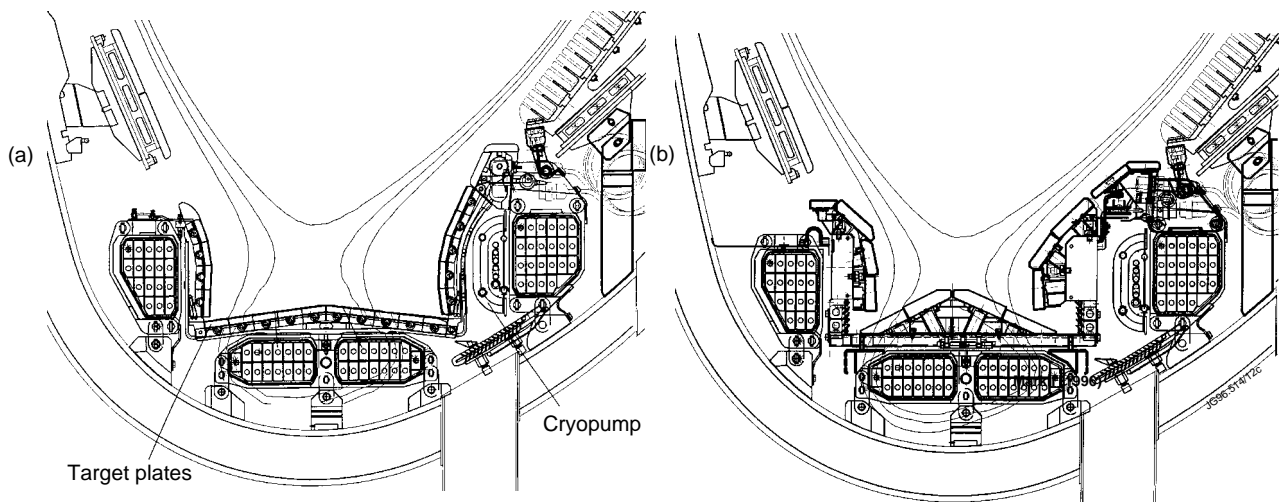
Figure 1.0.1 Poloidal cross sectional view of the JET Mark I (left) and Mark IIA(right) divertors.

Figure 1.0.2 shows a typical example of a radiative discharge in the Mk I divertor phase of JET (pulse #33204). This pulse shows the characteristic signatures of detachment when the radiated power fraction increases from 70 to 80%. In Mk I strike point sweeping at a frequency of 4Hz was used to increase the target wetted area. As a result the peaks seen in the ion saturation current in figure 1.0.2 represent complete profiles across each strike zone. The peak divertor ion-saturation current rolls over and reaches a level below that of the ohmic phase. Expanded

views of ion current show the underlying profile between ELMs with the ELM spikes superimposed. The central dip which appears at 18.95s corresponds to the private flux region.

With increasing P_{rad}, the ELM frequency increases and the amplitude declines which contributes to the reduction in peak ion flux during the ELM. As a result, it is not clear to what extent the ELMs are actually buffered by the gas target. The observation that detachment occurs with relatively small changes in radiated power fraction and density appears to be quite general. The divertor target power flux in the detached phase is too small to be detected by the IR camera but the Langmuir probes show that in #33204 about 6MW of power arrived at the target at 15s falling to around 1.5MW at 19s (assuming $T_i=T_e$).
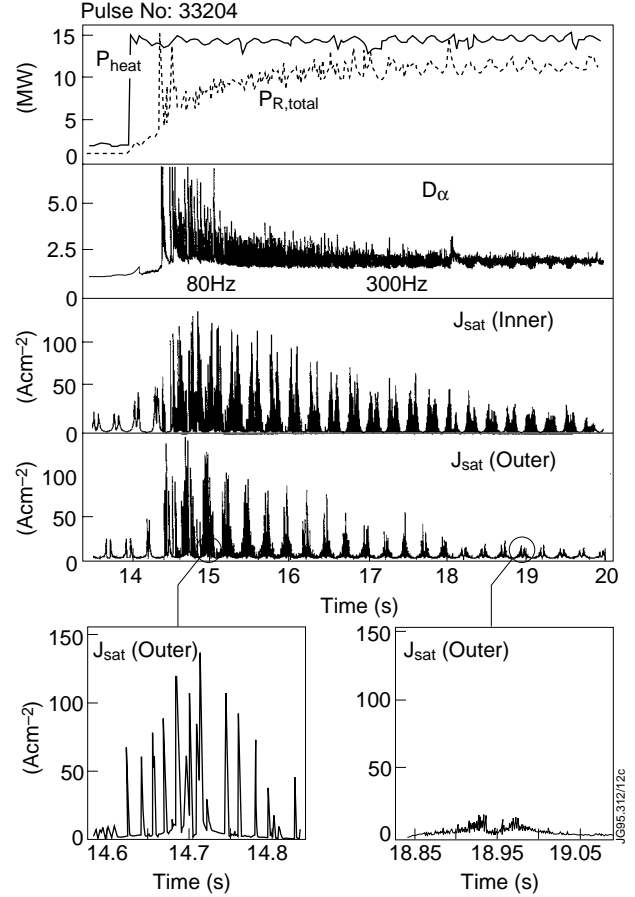

Figure 1.0.2 Typical radiative discharge in JET exhibiting partial detachment at outer and inner strike zones

1.1 Impurity content

In the example shown in figure 1.0.1 the impurity content (equivalent to $Z_{eff}=2.5$) is well above the ITER reference value which, excluding the contribution from helium ash ($\Delta Z_{eff}=0.2$), is: $Z_{eff} \leq 1.6$ [*Janeschitz*]. However, in radiative regimes where the radiated power fraction is being controlled, Z_{eff} is not a free parameter since sufficient impurity must be injected to achieve the desired level of radiative losses. What is critical for the viability of this regime is the radiative efficiency or more specifically the relationship between Z_{eff} and the total radiated power P_{rad} , plasma surface area, S, line averaged density, $\bar{n}_e$ and atomic number Z of the seed impurity. Multi-machine scaling of experimental data and data from code simulations has shown a remarkably simple and robust relationship between these parameters [*Matthews(1997)*] which in its approximate but most convenient form is:

$$Z_{eff} = 1 + 7 P_{rad} / (S\bar{n}_e^{2})$$ (1.1.1)

where P_{rad} is in MW, S in m^2 and $\bar{n}_e$ in units of 10^{20}m^{-3}. Similar behaviour is also observed for intrinsic impurities [*McCracken98*]

Using ITER parameters this expression predicts a Z_{eff} for ITER which is not too far above

3

the required value and certainly within the scatter of the data. Closed divertors were originally intended to allow high radiated powers within the divertor in conjunction with low core impurity levels. Recent data from the more closed JET Mark IIA and Mark IIAP divertor campaigns does not support this idea and is discussed in section 2.4

1.2 Energy confinement

Scaling laws are commonly used to compare the energy confinement in current machines and extrapolate to ITER but none has yet been created which is specific to the radiative regime planned for ITER. In this paper two scaling laws are quoted. The first is the ITERL89-P L-mode scaling which was developed for L-modes [*Yushmanov*]. With 100MW of additional heating, ITER can achieve its nominal fusion power if $H_{89L} = \tau_E / \tau_E^{89P} > 1.8$ (2.6 for ignition) [*Putvinski*]. A more recent scaling law is ITERH93-P which applies to ELM free H-modes [*ITER*]. This has the form:

$$\tau_{E,th}^{ELM-free} = \tau_E^{93H} = 0.036 m^{0.41} I_p^{1.06} R^{1.9} a^{-0.11} \kappa^{0.66} \overline{n}_e^{0.17} B^{0.32} P^{-0.67} \qquad (1.1.3)$$

where m[amu] is the mass of the plasma ions, I_p[MA] is the plasma current, R[m] is the major radius, a[m] the minor radius, κ is the elongation, $\overline{n}_e$ [$\times 10^{19}$m^{-3}] is the line averaged density, B[T] the magnetic field on axis and P[MW] the total heating power. On this H-mode scaling, ITER can achieve the nominal fusion power for $H_{93H} = \tau_E / \tau_E^{93H} > 0.68$ (0.85 for ignition) [*Putvinski*]. In the example of figure 1.0.2 the H_{93} factor reaches 0.68 which is marginal whilst H_{89} only reaches 1.5 which is below the ITER requirement. In extrapolating to ITER it is therefore critical to know which energy confinement scaling best describes these highly radiating plasmas. Although most radiative H-modes meet the minimum ITER requirements on the ITERH93-P scaling, no satisfactory JET points exist with $H_{89L}>1.8$ due to the less favourable ITER89P L-mode scaling.

In this paper the ITERH93-P scaling is quoted rather than the more recent ELMy H-mode scaling ITERH-EPS97(Y)[*Cordey*] since this is consistent with the existing publications which form part of this review. The difference between these two scalings is also rather small although ITERH-EPS97(Y) is slightly more favourable for ITER.

The dimensionless parameter or "wind-tunnel" approach to energy confinement scaling studies has put the empirical method of predicting the energy confinement in ITER on a sounder physical basis. Since the plasma geometry (shape, safety factor q_{95}), toroidal beta ($\beta \propto nT/B^2$) and collisionality ($\nu_* \propto nZ_{eff}L/T^2$) required by ITER can be achieved in current machines the standard approach used for type I ELMy H-modes [*Cordey*] is to keep these 5 dimensionless parameters fixed and scale the confinement with normalised ion gyro-radius ($\rho_* \propto T^{0.5}/BL$). To perform these ρ_* scaling experiments in JET the toroidal field was varied in the range 1-2.6T. Collisionality can be kept constant by varying n$\propto$B$^{4/3}$ which is achievable. This work has shown

that type I ELMy H-modes have Gyro-Bohm type scaling for which $B\tau_{E\,th} \propto \rho_*^{-3}$ (ITERH93-P: $B\tau_{Eth} \propto \rho_*^{-2.7}\nu_*^{-0.28}\beta^{-1.2}$) as opposed to the less favourable Bohm like transport for which $B\tau_E \propto \rho_*^{-2}$ (~ ITERL89-P). In section 3 the constraints on applying this dimensionless scaling approach to radiative discharges are discussed together with JET experiments in which this methodology has been applied. The results of this global approach are compared with local transport analysis (section 3.4) and finally with a more general global scaling which considers the effect of ELMs in degrading the edge pedestal (section 4).

1.3 Density Limit

Another critical issue for ITER is the operating density which must be achieved if the required fusion power and sufficiently clean radiating plasmas are to be achieved. The Greenwald density limit [*Greenwald*] is a purely empirical formula which was originally developed for L-mode limiter discharges. The expression for the Greenwald density limit is very simple:

$$\overline{n}_{e,GL} = 10^{14} I_p / (\pi a^2) \quad \text{[SI units]} \tag{1.3.1}$$

Although the expression for the Greenwald Limit is dimensionally incorrect it is commonly used. In the example pulse shown in figure 1 the line averaged density reaches 75% of the Greenwald value which is typical for JET in both unseeded ELMy H-modes and radiative discharges. ITER would like to operate at $1.13 \times \overline{n}_{e,GL}$ [*Putvinski*] which is well above the typical value in current devices. This requirement is mainly driven by the fact that near the ITER operating point the fusion power depends on the square of the density. Equation (1.1.1) also suggests that high density is required if clean radiating plasmas are to be obtained. However, in an ignited regime, where the power which has to be radiated is proportional to the fusion power, the density dependence will tend to cancel out.

2 IMPURITIES, RADIATION AND THE EFFECTS OF DIVERTOR GEOMETRY

2.1 Power balance

Seeded highly radiating plasmas are of interest to any next step tokamak reactor because target power loads must be compatible with the thermal limits imposed by the divertor target tile design. Limitations in the JET infra-red camera system used in these experiments at high densities [*Clement*] coupled with the relatively low surface power deposition in radiative discharges has meant that the surface power deposition could not be directly measured. However, in the Mk I divertor, sweeping of the inner and outer strike points across the arrays of triple probes was effective in producing complete profiles which were not strongly perturbed by the sweeping process provided the strike zones were not close to the divertor corners[*Monk*]. These profiles of divertor ion flux and electron temperature can be used to calculate the power balance which can

be compared with the global balance. A simple sheath model is used in which the parallel power density seen by the probes is $q_{//}[Wm^{-2}] = J_{sat}(7.8T_e + E_{rec})$ where $J_{sat}[Am^{-2}]$ is the probe ion saturation current density, the factor *7.8* is the sheath power transmission factor assuming $T_i = T_e[eV]$ and $E_{rec}=13.6eV$ is the recombination energy for each deuteron neutralised at the target surface. An example of this analysis is shown in figure 2.1.1 and relates to pulse 33204 whose time history has already been described in figure 1.0.1. This shows good power balance up to the time of 15.5s after which time the discharge begins to become detached (see next section).

The discrepancy in the target power later in the discharge appears to arise because the radiated power is calculated using the main chamber bolometer system. This diagnostic is screened from any neutral losses localised in
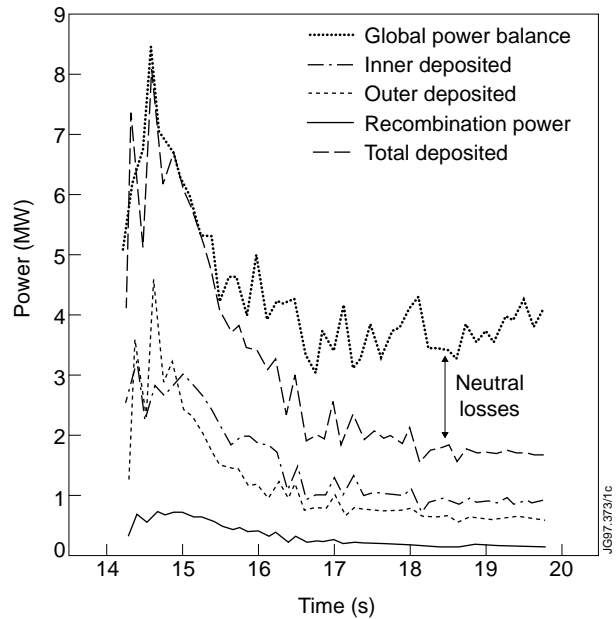

Figure 2.1.1 Comparison of the power deposited on the MkI divertor target for pulse 33204 (see figure 1.0.1) as derived from the Langmuir probes and the global power balance (main chamber bolometer system). Recombination power is the contribution to the target power from recombination of deuterons which strike the target surface.

the divertor by the core plasma [*Reichle(1997)*] and so is a measure of the electromagnetic losses alone. The probes on the other hand will be sensitive to the total charged particle power loss. An estimate of the neutral particle contribution to the power losses can also be made from a comparison of intersecting main chamber and divertor bolometer channels [*Reichle (1997)*], [*Ingesson*]. However, the absolute value of the neutral losses determined from the bolometer analysis is uncertain and so has been normalised to the probe data. A comparison between the neutral power losses implied by the probe data with that derived from the bolometer systems is shown in figure 2.1.2 and shows the same trend with the degree of detachment. Problems can sometimes arise with electron temperatures derived from probe data under detached conditions due to the effects of plasma resistivity [*Monk*]. However, all the known complicating factors in probe interpretation tend to increase the measured electron temperature and hence the calculated power above the true value, so the neutral power loss calculated from the probe data can be regarded as a lower limit.

When the total fractional power loss is calculated included both the electromagnetic plus neutral losses it reaches ~90% as shown in figure 2.1.3. This is more consistent with the fractional radiated powers reported for the CDH mode in ASDEX-Upgrade [*Kallenbach*]. There is also evidence from the divertor bolometer systems that the neutral losses have increased as the JET divertors have become more closed *[Ingesson]*. This would be consistent with the observa-

tion that the limit in the achievable electromagnetic radiated power fraction in seeded discharges has fallen in going from MkI(~80%) to MKIIa(~65%) and MkIIap(~60%).
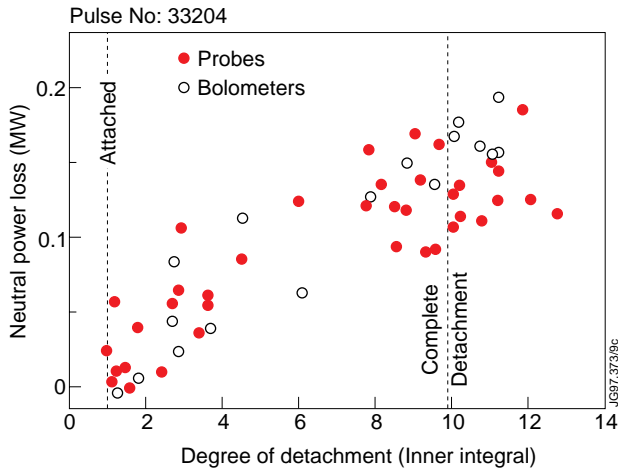

Figure 2.1.2 Estimates of the neutral power losses in the divertor for pulse 33204 derived from: 1) the differences between the Langmuir probe derived power and the global power balance and 2) from the discrepancy between divertor and main chamber bolometer chords plotted as a function of the degree of detachment (defined in section 2.3).
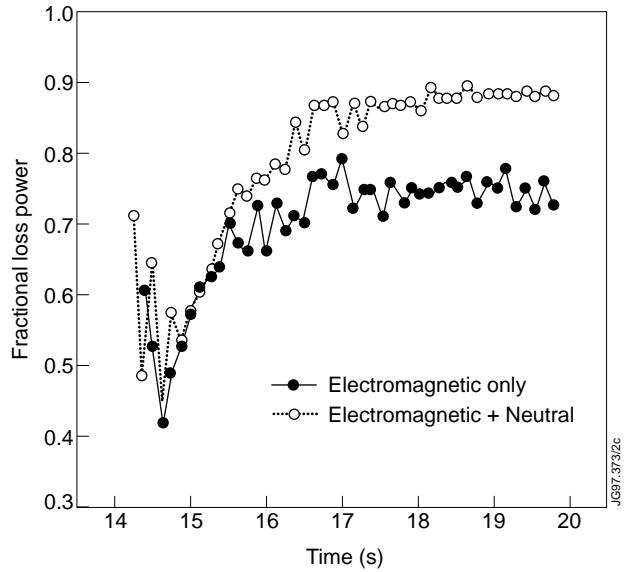
Figure 2.1.3 Radiated power fraction for pulse 33204 including and excluding the estimated neutral losses in the divertor.

Power balance calculations from the target Langmuir probe data in MkIIa and MkIIap appear less satisfactory than in MkI partly because the narrower divertor did not allow sufficient sweeping to completely cover the profile. However, if we use the attached ohmic phase to provide normalisation of the power balance then we find that just before the radiative limit when the electromagnetic losses have reached 65%, only 10% of the input power can be accounted for by the target probes suggesting a similar total radiative fraction to that seen in MkI (~90%).

2.2 Distribution of the radiative losses

In ITER it is planned that there will be 300MW of alpha heating plus auxiliary heating 100MW of which will be radiated from the core by Bremstrahlung. Of the remaining 200MW arriving at the plasma edge, 50MW are to be radiated in a plasma mantle inside the separatrix, 100MW will be radiated or lost due to neutral interactions in the divertor or SOL leaving 50MW to be deposited on the divertor targets[*Janeschitz*]. This is one of the main reasons for large fraction of the ITER machine volume currently dedicated to the divertor. In the JET MkI divertor detachment and large radiated power fractions are associated with the migration of the radiating region to the X-point [*Reichle(1995)*]. The more closed JET MkIIa divertor has not shown any change in

this picture although an increase in the number of divertor bolometer channels has meant that tomographic reconstructions are more precise [*Ingesson*]. Figure 2.2.1 shows tomographic reconstructions for four time slices from a MkIIa pulse (P_{heat}=12MW, I_p=2.5MA, B_t=2.5T) with deuterium fuelling (1.5×10^{22}electrons s^{-1}) and nitrogen seeding (3×10^{22}electrons s^{-1}). Electromagnetic radiated power fractions for each time slice are listed in table 2.2.1.
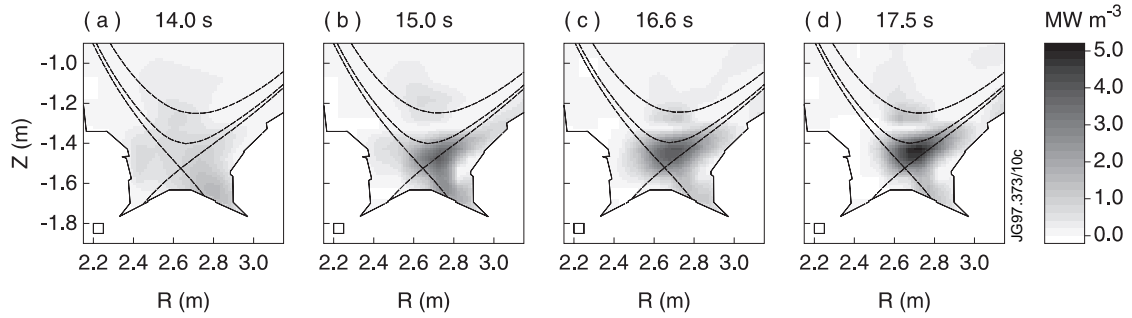

Figure 2.2.1 Radiated power distributions for MkIIa pulse 37991 from tomographic inversion of bolometer data. The radiated power fraction rises (see table 2.2.1) and the peak emission moves inside the separatrix just above the X-point.

Time (s)	Input Power (MW)	Total radiated power (MW)	Radiated power inside separatrix (MW)	Radiated power inside Ψ_{95}(MW)	frad, (%)	Inner DoD
14	12.1	5.3±0.5	3.3±0.5	2.2±0.3	43±4	2
15	12.7	8.3±0.7	4.9±0.5	3.0±0.4	65±6	11
16.6	13	9.1±1.0	5.6±0.7	3.2±0.7	70±8	21
17.5	13	9.5±1.2	6.2±0.7	3.2±0.7	73±9	19

Table 2.2.1: Quantitative assessment of electromagnetic radiated power from tomographic inversion of N$_2$ seeded pulse 37991. The input power during this interval was held constant at 12MW. The degree o^'etachment is also tabulated for each time slice (see section 2.3).

One can see from this table why the term "radiative divertor" is not very appropriate since at all times much of the radiation (~65%) comes from inside the separatrix. At all 4 times the electromagnetic radiation from below the X-point is 1±0.5MW (8%±4% of the input power). However, as discussed in the previous section this may be matched by neutral losses in the later phase of the discharge. The fraction of the input power radiated inside $\overline{\Psi}_{95}$ rises only slightly with impurity seeding from 18% to 25% of the input power.

An absolutely calibrated VUV survey spectrometer viewing the divertor region in the Mark I phase has shown good agreement with the main chamber bolometers when the powers measured in each of the observed spectral lines are summed together[*Maggi*]. In nitrogen seeded discharges, a typical breakdown of the loss channels for the detached phase gives ~85% of the

loss power from nitrogen ~10%, from carbon and ~5% from deuterium line emission [*Maggi*]. Figure 2.2.2 shows an example of such an analysis is shown for pulse 33204. Traces for the corresponding main parameters can be found in figure 1.0.2.

Increasing the Z of the seed impurity from nitrogen to neon and then argon increases the uniformity and depth of the radiating mantle inside the separatrix. In JET this can be seen from the radiation asymmetry factor defined by $f_R^{asym}=P_R^{asym}/P_R^{sym}$ where the symmetric contribution to the total radiated power is defined to be twice the total radiated power measured in the upper half of the plasma and $P_R^{asym}=P_R^{total}- P_R^{sym}$. For nitrogen seeded discharges $f_R^{asym} \sim 0.65$, for neon $f_R^{asym} \sim 0.5$ and for argon $f_R^{asym} \sim 0.35$ these factors are consistent with the results from tomographic reconstruction [*Reichle(1995)*]. In the situation where the seed impurity dominates, these factors show little dependence on plasma conditions.
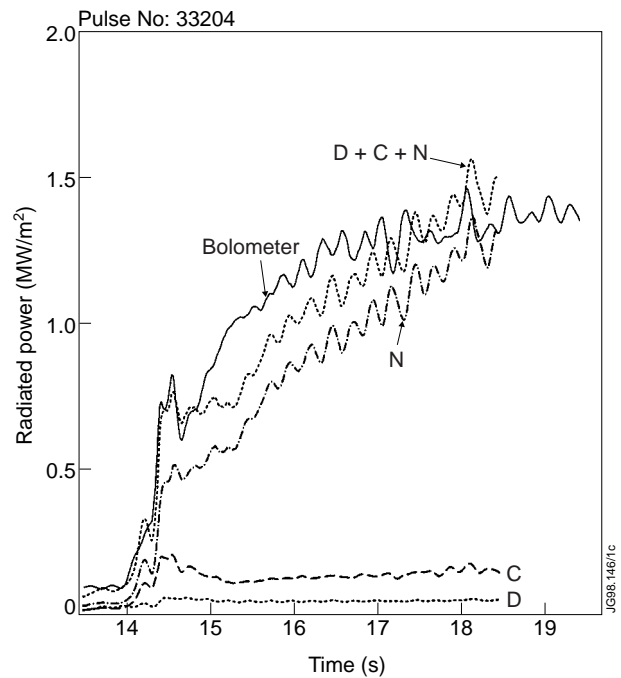

*Figure 2.2.2 Breakdown of total radiated power density between deuterium, carbon and nitrogen (D,C,N) seen by an absolutely calibrated VUV spectrometer for pulse 33204. Good agreement is shown with a similar bolometer line of sight also viewing the X-point region [*Maggi*]. Time histories for the main plasma parameters can be found in figure 1.0.2.*

2.3 Detachment

Figure 1.0.2 provides a qualitative view of the reduction in peak ion-flux to the divertor target produced by the introduction of deuterium and nitrogen impurities. This reduction in target ion flux can occur for a trivial reason such as a decrease in upstream density. To elminate this possibility a quantitative measure is required for the extent to which a discharge is detached. Strictly speaking this is defined by the degree to which the static plus dynamic pressure is conserved on flux tubes connecting the divertor target with the main chamber SOL [*Matthews(1995a)*]. The static pressure drop in the electron channel can be directly measured on JET using the outer target Langmuir probe systems and reciprocating probes in the main chamber SOL. An example of these measurements is given in figure 2.3.1 [*Loarte(1997a)*] for 3 cases: (a) an unfuelled type I ELMy plasma in which the parallel pressure is conserved between ELMs, (b) a discharge with strong deuterium fuelling in which there is a large loss of pressure balance between ELMs and (c) a discharge with strong nitrogen and deuterium puffing in which a large pressure drop is maintained over a substantial part of the profile. These measurements were made with triple probes with 100μs time resolution. Each profile represents a sweep of the

reciprocating probe or strike point over a period of about 100ms. For reference, ITER is thought to require an average parallel pressure drop of about a factor 10 [*Janeschitz*].
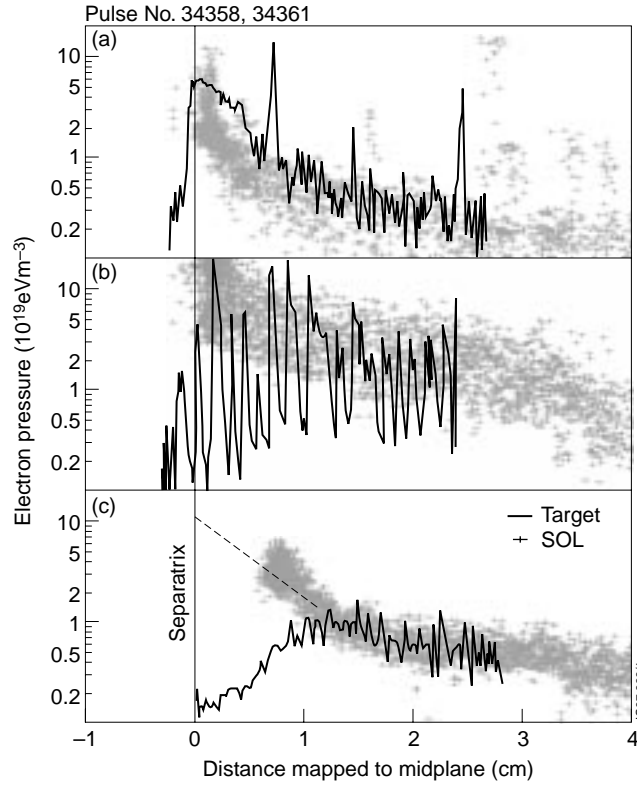

Figure 2.3.1 Electron pressure profiles at the target and in the SOL for 3 H-mode discharges (a) no gas fuelling, (b) strong deuterium fuelling showing detachment between ELMs and (c) deuterium plus nitrogen fuelling showing steady state detachment.

In JET, this type of data is available for relatively few discharges and so a more generally applicable definition of the degree of detachment (DoD) has been developed [*Loarte(1997a)*]. This is based on the principle that in the attached high recycling regime, at fixed input power, the target ion flux would be expected to rise as the square of the upstream density:

$$I_d^{scal} = C\overline{n}_e^2 / (1 - f_{rad})$$

where C is the constant of normalisation, $\overline{n}_e$ is the line averaged density measured near to the edge of the main plasma and f_{rad} is the fractional radiated power. The degree of detachment is then defined as:

$$DoD = I_d^{scal} / I_d^{measured}$$

where $I_d^{measured}$ is the ion flux measured by the divertor Langmuir probes. The upstream to downstream pressure ratio can be shown to be roughly equivalent in magnitude to the *DoD* and this

has been experimentally verified for radiative discharges. Figure 2.3.2 shows a comparison of the DoD vs (a) electromagnetic radiated power fraction and (b) fraction of the Greenwald density limit for the MkI, MkIIa and MkIIap configurations for the inner and outer divertor. These show that the discharges become very detached at lower electromagnetic fractional radiated power as the divertor becomes more closed: MkI(~80%) to MKIIa(~65%) and MkIIap(~60%). Although the actual density is about 10% higher in the MkI cases, the Greenwald density limit was also higher by a similar percentage due to slight differences in the plasma equilibrium. It therefore appears that closure did not reduce the density which was achieved with respect to the Greenwald limit. However, the confidence interval for this conclusion is about 10% due to difficulties in defining matched discharges given the differences in pumping, equilibria etc. between MkI and MkII. The impurity seeded radiative discharges have fractional Greenwald densities which are at most 10% lower than can be achieved with pure deuterium fuelling into discharges with the same triangularity [*Horton*].
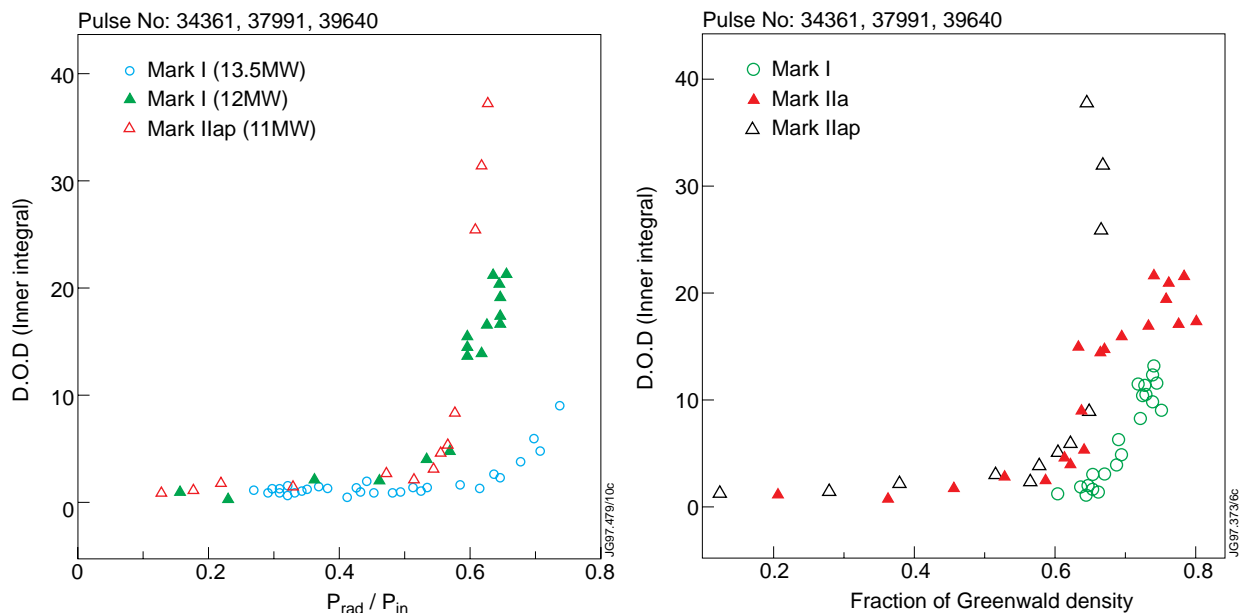

Figure 2.3.2 (a)Degree of detachment (DoD) vs electromagnetic radiated power fraction for the MkI, MkIIa and MkIIap divertors. Input power was 11-13.5MW with similar ratios of N_2 to D_2 fuelling. (b) DoD vs fraction of the Greenwald density limit for the same cases.

There is now good evidence that detachment in ohmic and L-mode discharges is closely correlated with the spectroscopic signatures of recombination [*McCracken97*]. The same is also true of radiative discharges where the ratio of the visible Balmer lines D_γ/D_α shows a sharp rise as the ion saturation current measured at the target rolls over and decreases, as shown in Figure 2.3.3. This change is characteristic of an increase in the relative population of upper states due to recombination which contrasts with what is seen with electron impact excitation alone which predominantly populates the lower levels. The fact that the D_γ/D_α ratio only reaches half way to that predicted for strong recombination my be related to the fact that the spectrometer views the target from the top of the JET torus and so line integrates through any excitation dominated

zones that lie above the recombining region. Limited time resolution of the diagnostics means that we cannot be sure that the signature of recombination is present during individual ELM events.
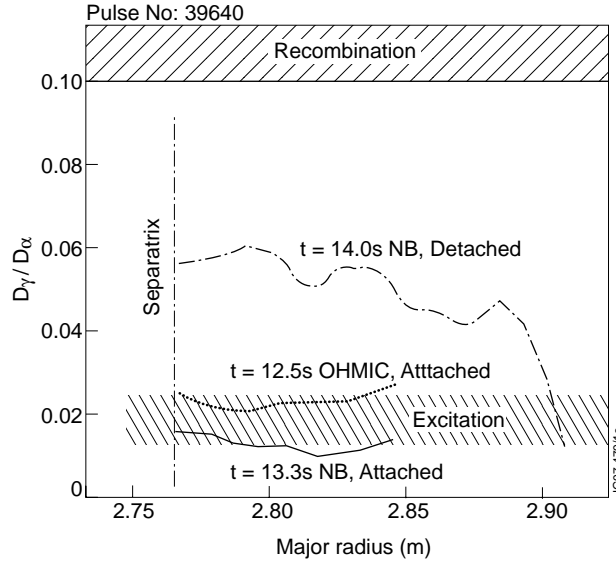

Figure 2.3.3 *Radial distributions of D_γ/D_α across the outer strike zones for pulse 39640 for the ohmic attached and H-mode attached and detached phases.*

2.4 Impurity Content

Data from the Mk0, MkI, MkIIa and MkIIap divertors has been analysed along with a multi-machine data set [*Matthews97*] using a fitting function relating Z_{eff} to the total radiated power P_{rad}, plasma surface area, S, line averaged density, $\overline{n}_e$ and atomic number Z of the seed impurity:

$$Z_{eff} = 1 + \alpha P_{rad} Z^\delta / (S^\beta \overline{n}_e{}^\gamma) \tag{2.4.1}$$

where α, β, γ and δ are determined by a non-linear least squares fit. The most recent result including the Mark II data is:

$$Z_{eff} = 1 + 4.5(\pm 0.4) P_{rad} Z^{0.12\pm0.04} / (S^{0.94\pm0.02} \overline{n}_e{}^{1.89\pm0.03}) \tag{2.4.2}$$

which is still well approximated by the simplified expression 1.1.1. The quality of this fit can be seen in figure 2.4.1 where only the JET data has been shown. In all cases Z_{eff}-1 is within a factor 2 of the scaling. The Mk0, MkIIa and MkIIap data all lies above whilst the MkI data is somewhat lower. This is why including the MkII data has made the prediction for ITER given by equation 2.4.2 slightly more pesimistic than the original fit [*Matthews97*]. Changes in the diagnostics between the MkI and MkII phases mean that it is hard to say whether this difference

12

is significant. The ITER reference operating point is also shown in figure 2.4.1 which is calculated from equation 2.4.2 assuming $S=1250m^2$, $P_{rad}=150MW$, $\overline{n}_e=0.96\times10^{20}m^{-3}$ and Ar impurity ($Z=18$).[*Putvinski*]. On this scaling ITER would have $Z_{eff}=2.25$ which means that the incremental Z_{eff} due to impurities other than helium is double what ITER requires ($Z_{eff}=1.6$). However, the requirement still lies within the scatter of the experimental data.

Detailed analysis of the JET Z_{eff} profiles reveals that in typical radiative discharges the profiles are slightly hollow such that:

$$(Z_{eff}^{central}-1) \, / \, (Z_{eff}^{line}-1) \approx 0.75 \pm 0.1 \tag{2.4.3}$$

where $Z_{eff}^{central}$ is the central value of Z_{eff} and Z_{eff}^{line} the line averaged value both determined from charge exchange recombination spectroscopy of all major impurity species. Although it is not clear how this might scale to a larger machine such hollowness would be beneficial to ITER since the fusion power will be a maximum where the Z_{eff} is lowest.
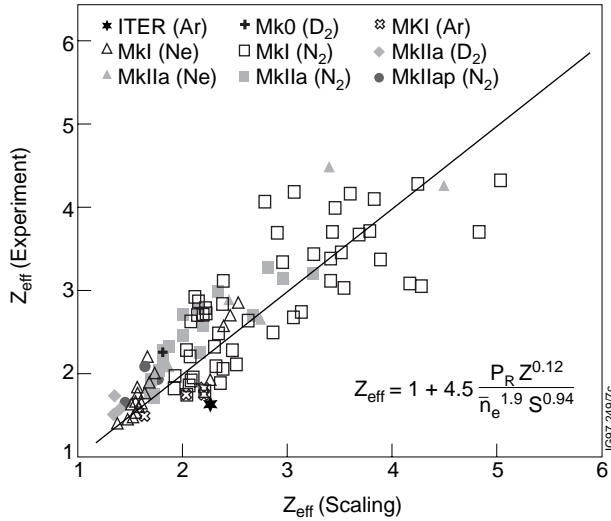

Figure 2.4.1 JET data for Mk0, Mk I, MkIIa and MkIIap divertors plotted against the multi-machine Z_{eff} scaling of equation 2.4.2.

In the original radiative divertor concept it was hoped that both the majority of the radiation and impurities could be kept in the divertor below the X-point. Since we have already shown in section 2.2 that the majority of the radiated power comes from just inside the separatrix it is perhaps not surprising that there is no evidence for a large increase of core impurity concentration when the plasma detaches. To make such comparisons within the database we define the ratio of the incremental Z_{eff} predicted by the scaling law to that measured by:

$$H_{zeff}=\{Z_{eff}\,(scaling)-1\}/\{Z_{eff}(experiment)-1\} \tag{2.4.4}$$

where the simplified scaling law of equation 1.1.1 is used. Defined in this way, large H_{zeff} is good because it means that more radiation is achieved for a given increment in Z_{eff}. Figure 2.4.2 shows the dependence of H_{zeff} on the electromagnetic radiated power fraction for a series of 2.5MA/2.5T discharges in the MkIIa divertor with 12MW of neutral beam heating. Points are also identified according to the plasma equilibrium that was used. Standard flux expansion cases correspond to an expansion factor of 6.5 measured between the 1cm flux surface at the outer mid-plane and the outer divertor, normal to the flux surfaces. High flux expansion cases have an

expansion factor of 12. Results indicate that discharges run on the vertical targets have a slightly higher H_{zeff} than the horizontal standard flux expansion equilibria which in turn perform better

than the horizontal high flux expansion cases which have the lowest H_{zeff}. In any given configuration there is rather little variation in H_{zeff} with fractional radiated power. It seems most likely that the variations are due to changes in the edge temperature and density distribution which influence the radiative efficiency. Code calculations have not predicted any significant enrichment of the divertor impurity concentration with respect to the main chamber and this is consistent with the experiment in that there is no evidence for any significant reduction in H_{zeff} at high radiated power fractions where the detachment occurs.
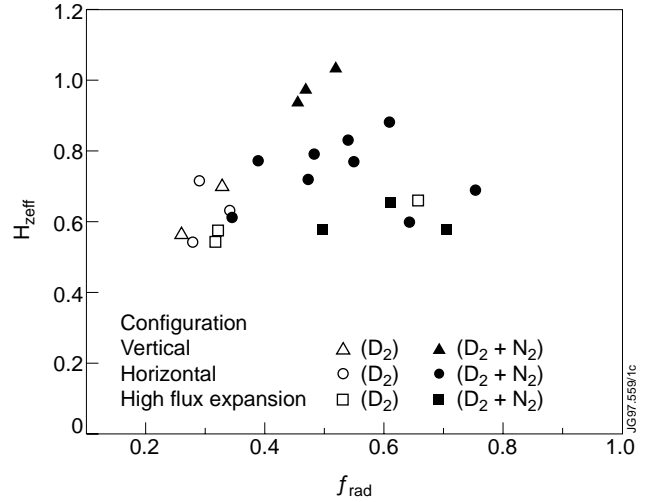

Figure 2.4.2 H_{zeff} *(defined by eqn. 2.4.4) for 3 different plasma equilibria in the MkIIa divertor plotted against the electromagnetic power fraction f_{rad}.*

2.5 Code Simulations

Two code combinations have been used at JET for the simulation of the edge plasma in radiative regimes. Most generally applicable for detached regimes is the EDGE2D multi-fluid code coupled with the NIMBUS Monte-Carlo code for neutrals [*Taroni*]. However, the DIVIMP Monte-Carlo impurity ion transport code [*Stangeby*] has also been used in combination with NIMBUS run on "onion-skin" plasma models linked to target probe data or plasma backgrounds generated by EDGE2D.

In simulating experimental data, EDGE2D is run with radiation feedback such that the impurity puff rate is adjusted by the code until a specified radiated power fraction is achieved. Transport coefficients are then manipulated until both the target Langmuir probe data and upstream profiles measured with the reciprocating probe are well matched. As a consequence, the degree of detachment in the simulation matches that in the experiment although the code tends to be more asymmetric in solutions with a more strongly detached inner target than the experiment. The matching of the target profiles predicted by the code with those from the experiment (for example, figure 2.3.1) leads to relatively large values for the transport coefficients ($D_{\perp}=0.4m^2/s$ and $\chi_{\perp}=2.5m^2/s$) as compared with those used in modelling the inter-ELM periods of unfuelled ELMy H-modes ($D_{\perp}=0.05m^2/s$ and $\chi_{\perp}=0.2m^2/s$). This transport enhancement may be attributed either to the fact that the high frequency ELMs are not considered in the modelling or connected with the increase in transport seen at low edge electron temperatures even in L-mode [*Erents*].

14

The distribution of the radiation predicted by the code shows much finer structure than is seen in the tomographically inverted bolometer data. To make a meaningful comparison a diagnostic simulation of the EDGE2D output is required which calculates what would be seen by the JET bolometer system. This can then be tomographically inverted in the normal way and directly compared with the inverted experimental data, as shown in figure 2.5.1 for a nitrogen seeded discharge in Mk I with 80% fractional radiated power [*Ingesson*]. The bolometer system in the MkIIa divertor phase had higher spatial resolution but an equivalent comparison has not yet been made.
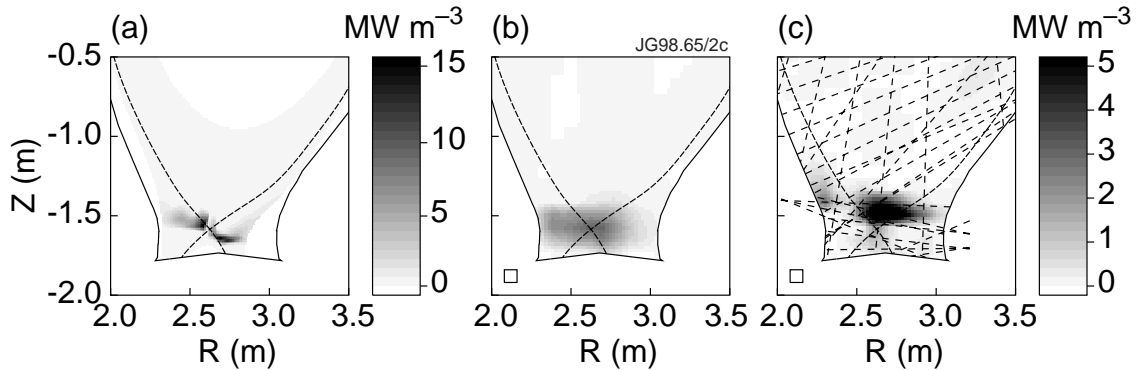

Figure 2.5.1 Pulse 34361 at 55.6s (as figure 2.3.1(c)) (a) EDGE2D simulation of nitrogen and deuterium radiative losses, (b) radiated power distribution from tomographic reconstruction of the simulated bolometer views of the EDGE2D data and (c) radiated power distribution from tomographic reconstruction of the experimental bolometer data with bolometer lines of sight overlaid. The squares indicate the grid size used in the reconstructions.

The radiation in the experiment is further inside the separatrix and more peaked than in the simulation. A slight rise in the radiated power fraction requested in the simulation can produce a radiating region inside the separatrix which is a better match to the experiment. However, these solutions are not stable since the radiating region moves upward and inward to the edge of the computational grid adjacent to the core and triggers a collapse in the solution. The fact that the experiment seems more robust than the model may be attributed to the rapid ELMs which have been shown in similar B2/EIRENE simulations of neon seeded ASDEX-Upgrade discharges to have a strong stabilising influence on the X-point MARFE [*Schneider*].

Predictive runs, i.e. not matched to specific pulses, have also been carried out using DIVIMP/NIMBUS and EDGE2D/NIMBUS to test the multi-machine Z_{eff} scaling of equation (2.4.2) for a variety of machines and a wide range of assumptions about the plasma conditions [*Matthews(1997)*]. This result is shown in figure 2.5.2. The simulations show a similar level of consistency to the Z_{eff} scaling law as the experiment and since ITER simulations are also included one can have greater confidence in such an extrapolation. There is still no adequate theoretical explanation as to why the Z_{eff} scaling law works as well as it does. The DIVIMP simulations show that the electron density, impurity density and impurity radiation function within the radiating volume as well as the size of the radiating volume can each vary by up to an

order of magnitude depending on the assumptions made about the background plasma. Surprisingly however, the product of these quantities tends to remain approximately constant which is the condition for the simple scaling law to hold. If the scatter in these parameters were uncorrelated the deviation from the scaling prediction would cover 4 orders of magnitude!

Whilst there is good overall agreement between code simulations and experiment for the primary plasma parameters the details which are closely linked to the atomic physics are less well characterised. For example, the compression factor for the nitrogen in MkI pulse 34361 was measured to be 15±5 [*Ehrenberg*] which compares well with the

Figure 2.5.2 Z_{eff} *from a wide variety of EDGE2D and DIVIMP predictive runs versus the* Z_{eff} *scaling law, equation (2.4.2).*

factor 20 seen in the simulation [*Loarte*]. However, the actual nitrogen concentrations predicted by the code are a factor 3 too low and the radiated power is predicted to come equally from *NIV* and *NV* radiation whereas in the experiment a VUV spectrometer, which can account well for the radiated power, shows *NV~2×NIV*[*Maggi*]. In general, it is not clear to what extent such discrepancies are due to uncertainties which are known to exist in the atomic data for nitrogen as opposed to inaccuracies in the simulation of the electron temperature and density distributions in the plasma or in the plasma transport.

3. ENERGY CONFINEMENT

3.1 ρ_* Scaling in Radiative Regimes

Matching of the three parameters ρ_*, ν_* and β should ensure that all plasma physics phenomena, including collisional effects with Coulomb-like cross-sections are scaled correctly [*Connor*]. It has been shown [*Lackner*] that atomic physics effects such as radiation, charge exchange and other ion-neutral interactions of importance in the plasma edge can only be scaled when the absolute temperature, T, is also matched. Detachment occurs when the divertor temperature falls to a few *eV* or less [Loarte]. In JET, detached divertor plasmas are obtained at similar values of total fractional radiated power f_{rad} for a wide range of conditions and so f_{rad} has been used as a closely related alternative dimensionless parameter. Using lower *Z* impurities (nitrogen and neon) the radiation distribution will be more similar to that expected in ITER for argon. Fixing f_{rad} also
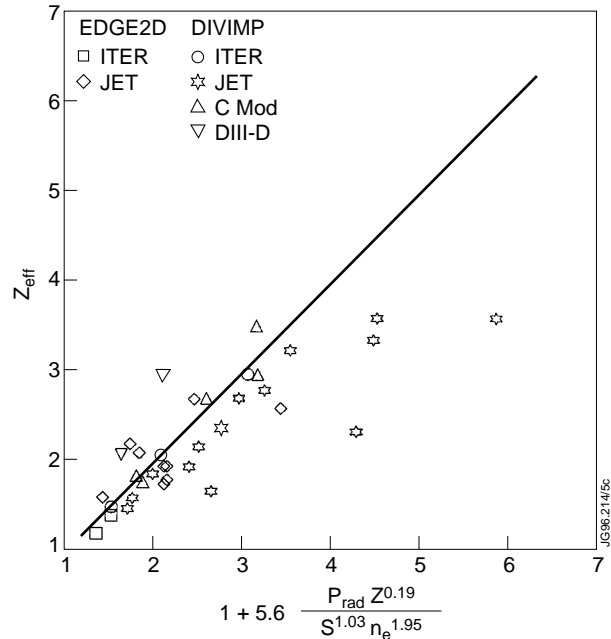
16

avoids any confusion between changes in confinement and direct radiative losses from within the core plasma.

3.2 Constraints

In the JET experiments [*Stork*] q_{95}(3.1) , f_{rad}($\approx$60%), β($\approx$1.2) and Z_{eff}($\approx$3) were kept constant. Fractional radiated power $f_{rad}=P_{rad,total}/P_{heat,total}$ can be written in terms of Z_{eff} and line averaged density n by using the simplified Z_{eff} scaling of equation (1.1.1). P_{heat} can then be substituted with an expression in terms of dimensionless parameters via an appropriate confinement scaling law: Gyro-Bohm $B\tau_E \propto \rho_*^{-3}$(~ ITER93H) or Bohm $B\tau_E \propto \rho_*^{-2}$(~ ITER89L). These relationships then imply to ensure similarity key parameters are constrained as follows:

Gyro-Bohm	$n \propto B^{6/7}$	$n/n_{Greenwald} \propto B^{-1/7}$	$\nu^* \propto B^{-10/7}$	$\rho^* \propto B^{-3/7}$	$P_{heat} \propto B^{12/7}$
Bohm	$n \propto B$	$n/n_{Greenwald}=$ const.	$\nu^* \propto B^{-1}$	$\rho^* \propto B^{-1/2}$	$P_{heat} \propto B^2$

Ideally we would find a means to keep n_* constant and one possibility might be to allow Z_{eff} or b to vary but it turns out that the required parameter variations either do not exist or are impractical. Fortunately the n_* dependence of the commonly used confinement scalings is rather weak ($B\tau_{EH93} \propto n_*^{-0.28}$, $B\tau_{EL89} \propto n_*^{-0.12}$, $B\tau_{EH97} \propto n_*^{-0.08}$) so that the failure to maintain constant n_* may have only a small effect on the results. Another useful feature of keeping f_{rad} constant is that required density dependence equals or is very close to a constant with respect to the Greenwald density limit. This is also convenient since although the Greenwald limit is not dimensionally correct there is good empirical evidence that the proximity to this limit can strongly influence confinement [*Asakura*].

3.3 Global Confinement Scaling

Figure 3.3.1 shows the variation of the $H_{ITER93-H}$ factor with ρ_* from the JET series of radiative ρ_* scaling experiments [*Matthews97b*]. Data have been restricted to pulses with f_{rad}>50% and multiple points have been taken from two pulses for each value of toroidal field. Data from radiative discharges in ASDEX-Upgrade and DIII-D is also included although these are not identity pulses that match exactly the JET dimensionless parameters and plasma shape. All these data are consistent with a degradation with respect to the Gyro-Bohm like (ITERH93-P: $B\tau_E \propto \rho_*^{-2.7}$) scaling as ρ_* decreases. The radiative pulses are better described by $B\tau_E \propto \rho_*^{-1.7}$ as shown in figure 3.3.1. This is in contrast to the type I ELMy H-modes [*Cordey*] which are also shown.

Figure 3.3.2 shows variation of ν_* with ρ_* for the same data. Although ν_* cannot be held constant in these discharges the existence of similar $H_{ITER93-H}$ factors for widely differing ν_* indicates that the confinement is weakly dependent on collisionality as is characteristic of existing scaling laws. There also appears to be no strong beta dependence.
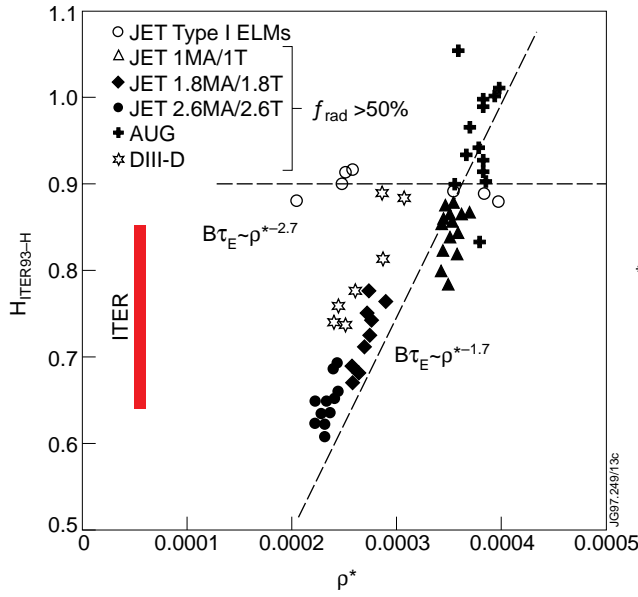
Figure 3.3.1 H_{93} vs ρ_* for H-modes with $f_{rad}>0.5$ [Matthews97b] compared with unseeded JET type I ELMy discharges [Cordey].
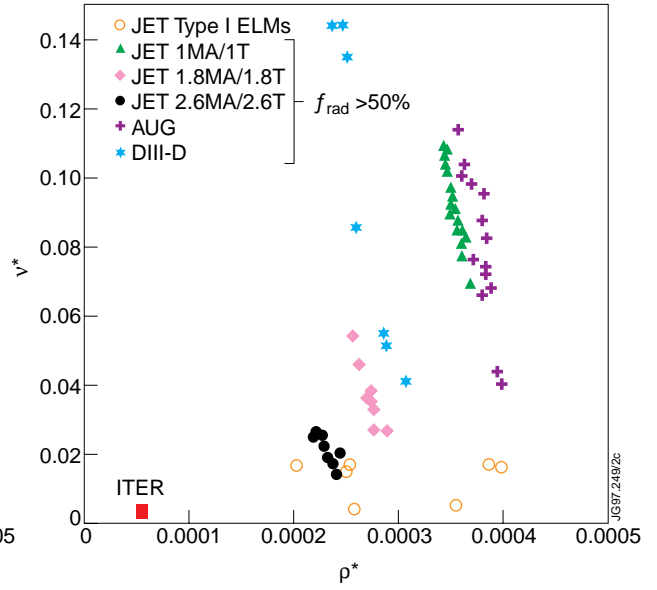
Figure 3.3.2 ρ_* vs υ_* for H-modes with $f_{rad}>0.5$ compared with unseeded JET type I ELMy discharges [Cordey].

Regression of the energy confinement time for the JET, DIII-D and AUG discharges with $f_{rad}>0.5$ against a dimensionally correct expression gives:

$$B\tau_E = 8.2 \times 10^{-8} \rho_*^{-1.7} \nu_*^{-0.25} \beta^{-0.14} \qquad (3.3.1)$$

The ρ_* dependence lies somewhere between the Bohm and Goldston like scalings. Since the ν^* dependence is similar to that of ITERH93-P this scaling with ρ_* has been represented in figure 3.3.1. Although expression *3.3.1* fits the confinement of the radiative discharges for $f_{rad}>50\%$ with a scatter around the fit of ~20% it cannot be assumed to be generally applicable. As the ELM frequency varies, discharges can evolve along a path which is orthogonal to the scaling line. In subsequent sections we will demonstrate that the globally Bohm like appearance appears to be the result of changes near the edge of the plasma which mask what is happening in the core. A more generally applicable confinement scaling law which separates out the effects on pedestal and core is described in section 4.2 and can reconcile both radiative and non-radiative discharges.

Successful operation of ITER will require both high energy confinement and high density. JET experience in low triangularity type I ELMy H-modes is that with deuterium gas fuelling, the density can be raised up to about 70% of the Greenwald value at which point the confinement becomes increasingly degraded [*Horton*]. A useful figure of merit accounting for the need to simultaneously achieve both high density and energy confinement is the product $H_{93}\overline{n}_e / n_{GDL}$. Figure 3.3.3 shows a plot of this figure of merit vs normalised plasma density. Saturation occurs at a value of around $H_{93}\overline{n}_e / n_{GDL} =0.6$ for low triangularity type I ELMy discharges and 0.5 for seeded radiative cases ($f_{rad}>0.5$). ITER requires a value of 0.75 for its driven mode and 0.95 for

ignition. From figure 3.3.3 one can see that the confinement of the radiative discharges, all of which have rapid type III ELMs, is reduced by ~25% with respect to the deuterium only cases. At the very highest density $H_{93}\overline{n}_e / n_{GDL}$ saturates for the deuterium only cases and the points for radiative and non-radiative cases merge. This is consistent with a degradation of the edge pedestal as discussed in section 4.
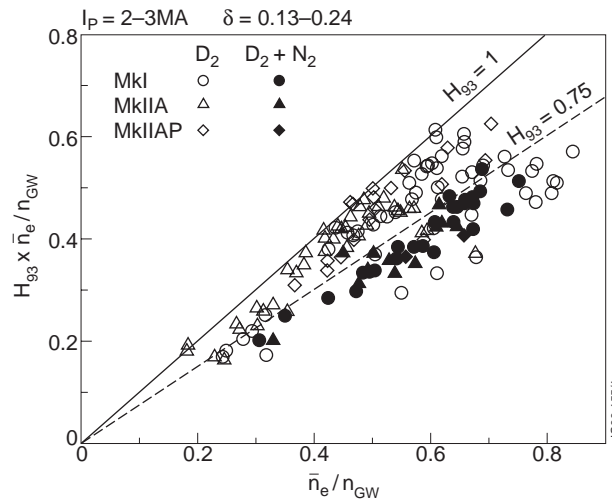

Figure 3.3.3 Comparison of the figure of merit $H_{93}\overline{n}_e / n_{GDL}$ for the various JET divertor phases for D_2 fuelled and nitrogen seeded radiative pulses with $f_{rad}>0.5$. Pulses were selected to be low triangularity ($\delta=0.13$-0.24) with plasma current in the range 2-3MA.

3.4 Local Transport Analysis

Local transport analysis of radiative JET pulses ($f_{rad}>50\%$) has been carried out using the TRANSP code. Profiles of n_e, T_e, T_i, P_e, total thermal pressure P_e+P_i and χ_{eff} (dominated by χ_i) are shown in figure 3.4.1. In all cases the discharge parameters were: I_p= 2.5MA, B_T=2.5T with 12MW of neutral beam heating. A reference unfuelled type I ELMy discharge is compared to discharges seeded with nitrogen impurity. In one of these cases (37997) the density fell due to the loss in confinement but in the other (37991) strong D_2 fuelling was used to maintain the density. Due to its lower density N_2 seeded pulse 37997 has more or less the same temperature as the unseeded type I reference 38287. Hence once can see from figure 3.4.1(f) that in going from an unseeded to seeded discharge at similar ρ^*, the core χ_{eff} is increased. If the density is maintained by deuterium fuelling then the core χ_{eff} remains more or less constant whilst there is a significant increase in χ_{eff} outside q=2.

The apparent decoupling of the core and edge confinement are not obviously consistent with confinement models in which the edge and core confinement are strongly linked [*Kotschenreuter*]. Also, the electron temperature profiles shown in figure 3.4.1(b) do not appear to show the strong profile resilience reported by ASDEX-Upgrade [*Gruber*]. The common feature of the JET profiles is that the core electron pressure profiles have the same gradient for both
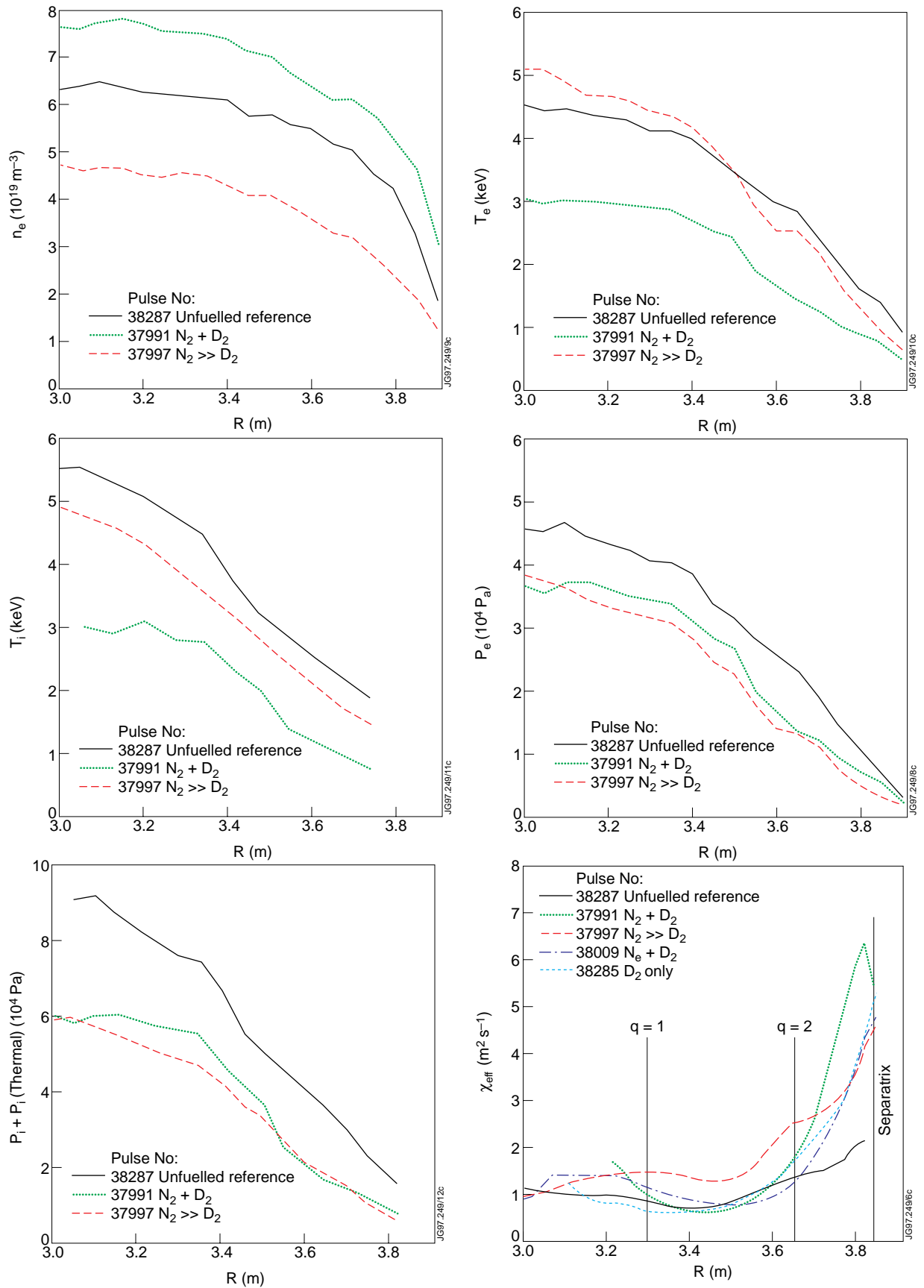
Figure 3.4.1 (a) to (e): Profiles for an unfuelled type I ELMy reference discharge (38287) compared with a radiative discharge with strong N_2 and D_2 injection (37991) and lower density discharge with N_2 injection and very little D_2 fuelling (37997). Frame (f) shows the χ_{eff} profiles for a wider range of radiative discharge and an unfuelled reference.

unfuelled and fuelled or impurity seeded discharges. One can see from the examples given that the electron temperature profile can be altered but that the pressure profiles appear to be simply shifted down by an amount corresponding to the change in the edge pedestal.

In radiative discharges there may be a concern that the increase in χ_{eff} near the edge is merely the result of direct losses which have not been correctly accounted for in the analysis. However, as was demonstrated in table 2.2.1, tomographic inversion of the bolometric data shows that the majority of the radiation is emitted from outside the ψ_{95} flux surface [*Ingesson*] and as a result, the derived χ_{eff} is very insensitive to the assumptions made about the radiation profile. Monte-Carlo calculations of the charge exchange losses coupled with bolometric evidence show that these losses are too small to influence the transport analysis and in any case are mainly located outside q_{95}.

We would like to know how the χ_{eff} in the core scales with ρ_*. However, to do this with constant collisionality and beta in discharges with similar radiative losses is not possible for the same reasons as for the global scaling. In addition, one should strictly use local definitions of the dimensionless quantities. Without a specific transport mechanism in mind it is not obvious which length scale to use in the definitions. New parameters based on local gradients might be more relevant but experimental errors would make the scatter in such quantities too large to be of use. As a result a simple but practical definition of ρ_* has been used. The ion gyro-radius has been calculated using the local ion acoustic speed $c_s \propto (T_i + T_e)^{0.5}$ and the result normalised by the minor radius. Figure 3.4.2 shows a logarithmic plot of χ_{eff}/B vs ρ_* for all the impurity seeded discharges which have been investigated with the TRANSP code. A reference case and a discharge strongly fuelled with deuterium only are also included. The χ_{eff} and ρ_* values were all extracted for the same radius (R=3.5m) which corresponds to the part of the plasma between q=1 and q=2 where the χ_{eff} profiles are fairly flat. The error bars represent the scatter of the data over a typical period of several seconds where the discharge conditions are in quasi-steady state (slow evolution on time scales $\gg \tau_E$). Regression of all the points corresponding to impurity seeded discharges leads to $\chi_{eff}(3.5m)/B \propto \rho_*^{2.9\pm0.04}$ which is indistinguishable from the Gyro-Bohm line shown on the plot. The statistical error on the exponent is however not really representative of the real uncertainties a better impression of this is obtained by comparing the exponent at various radii outside the sawtooth inversion radius (3.3m) as listed in table 3.4.1. This shows that the tendency is towards Gyro-Bohm like scaling up to 3.65m while it is more Bohm or Goldston like further out. In reality the uncertainties in the edge region are rather large since the exponent of fit is sensitive to which pulses are included or excluded from the fit. However, qualitatively the result is unaffected.

Some caution is required in comparing local transport in seeded and unseeded regimes because it almost certainly invalidates the dimensionless parameter approach which requires that the particle and energy source and sink profiles are matched. If the radiative cases are considered as a group they fit quite well to the Gyro-Bohm scaling in the core, particularly if we

select pulses 37991, 38605, 38608 and 38612 which have the best match in terms of seeding regime and have very similar normalised temperature profiles.

Radius (m)	Exponent for ρ_*
3.35	2.5±0.03
3.45	2.7±0.02
3.55	2.85±0.04
3.65	2.6±0.05
3.75	1.6±0.08

Table 3.4.1: Exponent (γ) for the ρ_* dependence of χ_{eff} at various radii between the sawtooth inversion radius and the plasma edge (~3.8m). A function of form $\chi_{eff}(r)/B \propto \rho_*^{\gamma}$ is fitted to the TRANSP data at each radius where B is the magnetic field on axis.
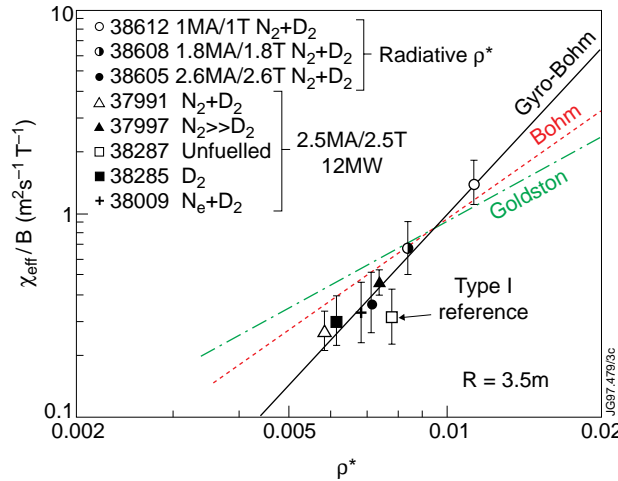

Figure 3.4.2 . Logarithmic plot of χ_{eff}/B vs ρ_* at R=3.5m for all the impurity seeded discharges which have been investigated with the TRANSP code. An unseeded reference (38287) and a pulse with strong deuterium puffing (38285) are also included.

4. EDGE OPERATIONAL SPACE

4.1 Discharge trajectories

Edge operational space diagrams describe the trajectory of a discharge in terms of pedestal values of n_e and T_e at the top of the H-mode pedestal[*Gruber, Keilhacker*]. The upper limit in edge pressure reached by type I ELMs before they crash is thought to be related to the critical pressure gradient for the ideal ballooning instability. The actual peak edge pressure reached during an ELM cycle therefore also depends on the pedestal thickness. In JET the density dependence of this upper pressure limit is consistent with a pedestal thickness Δ which scales

according to a "mixed model" $\Delta \propto \{a\rho_i\}^{1/2}$ [*Lingertat*] where it has been assumed that $T_i \propto T_e$. In edge operational space this implies that at the top of the pedestal the temperature scales as $T_e \propto n_e^{-4/3}$ [*Keilhacker*]. Figure 4.1.1 compares this upper boundary from nitrogen seeded discharges where the type I ELMs reappear after the impurity seed is switched off, with a series of unfuelled and deuterium fuelled discharges [*Keilhacker*] (2.5MA, 2.5T with 12MW of NB heating).

The lower limit in pressure to which the type I ELMs crash is also shown in figure 4.1.1 and appears to be more consistent with a line of constant pressure [*Fishpool*]. This lower boundary defining the depth of the ELM in-duced pressure crash is not yet understood. In the phase of the discharges where there are rapid small ELMs which are labelled as type III in figure 4.1.1 the minimum pressure is the same as for the type I ELMs. Strictly speaking this categorisation of the ELMs requires the relationship between the ELM frequency in-put power to be tested. However, the ELMs labelled as type I show a decline in frequency as the radiated power fraction rises whilst those labelled type III increase in frequency with ra-diated power fraction. Unlike the type I ELMs the type IIIs have much more horizontal tra-jectories as a result of oscillations in density and do not depart significantly from the lower pressure limit.

Figure 4.1.1 Diagram of JET edge operational space showing for nitrogen seeded discharges which evolve from large type I ELMs to small frequent (typeIII) ELMs. The upper and lower pressure limits for the large ELMs are consistent with those for D_2 fuelled and unfuelled type I ELMy discharges.

The edge temperature at which the L to H threshold occurs is around 800eV and this is believed to be independent of density [*Righi, Chankin*]. At high density the radiative discharges are pushed down the constant pressure line towards the L to H threshold temperature. However, most of the points seem to sit well above the 800eV level at which a back transition would be predicted.

4.2 Edge Pedestal and Implications for Global Confinement Scaling

The electron pressure profiles of figure 3.4.1(d) are typical of the observation that the edge pressure is reduced and that the core profile is simply shifted downwards by this amount. This observation fits in with the concept of an edge pedestal. The metaphor of the edge pedestal originates from the fact that provided the core transport is a relatively weak function of local
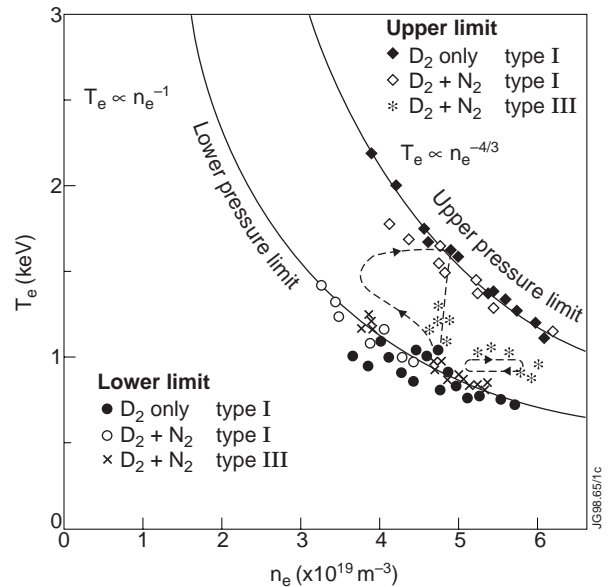
density and temperature, the pressure across the whole of the core plasma can be raised by the average pressure set at the boundary.

At present it is not clear what is the correct scaling for the pedestal thickness [*Lingertat*] but the implication of the $\Delta \propto \{a\rho_i\}^{1/2}$ scaling is a weak decrease in pedestal pressure with increasing pedestal density. If one were to stay exactly on this ballooning boundary then in a typical fuelling scan for which the pedestal density doubles this scaling implies a 6% reduction in total stored energy, assuming that this energy can be divided into roughly equal and independent contributions from the pedestal and core. However, the degradation is enhanced by the fact that as the ELM frequency is increased the time spent near the ballooning limit decreases. Hence the time averaged pedestal pressure departs increasingly from the ballooning limit as the ELM frequency is driven up by fuelling of deuterium and/or impurities. Finally, the rapid type III ELMs do not even reach the type I limit leading to a further drop in pedestal pressure.

Fishpool has proposed an explanation for the observed variation of confinement with gas puffing [*Fishpool*] based on a more detailed consideration of the cycles in edge pressure associated with ELMs. In an ELM-free H-mode plasma, of order half of the thermal energy can be ascribed to the pressure at the top of the pedestal and this pressure is controlled by the ELM behaviour. At high ELM frequencies, the (electron) pressure pedestal can be reduced by over 50% within ~1ms. Surprisingly the minimum pressure (measured at $\rho \approx 0.92$) after an ELM is almost independent of ELM frequency, for radiative plasmas observed in JET. Hence, with fixed power available to reheat the edge region, increasing the ELM frequency leads to a lower average pedestal pressure, and reduced energy confinement. By combining the assumptions of a lower limit to which the edge pressure always crashes with a reheat model for the pedestal region between ELMs, this model avoids the need to explicitly consider the scaling of the upper pressure limit.

On the basis of these observations, one can derive a dimensionless expression for the relationship between the ELM frequency, and the confinement enhancement [*Fishpool*]:

$$H = H_{\max} - a.f\tau_E\left(1 - e^{-b/(f\tau_E)}\right) \qquad (4.2.1)$$

where, $H_{\max}$ is the ELM-free confinement enhancement for a given plasma configuration and heating scenario, f is the ELM frequency, with a and b determined from the experiment. The plasmas of the type shown in figure 3.4.1 give values of a=0.031, b=14, with $H_{\max}$ given by the ITER-93 ELM free H-mode scaling law. Figure 4.2.1 compares the experimental values of H_{93} with the model values from equation (4.2.1) for a series of discharges in which only the deuterium and impurity fuelling rates were varied. Parameters a and b do not appear to vary significantly with plasma current.

An important implication of the assumptions leading to equation (4.2.1) is that the normalised ELM size defined as the fractional loss in stored energy per ELM is given by:

24

$$\Delta W / W = \left(1 - e^{-1/(f \tau_E)}\right) \qquad (4.2.2)$$

Combining this with equation (4.2.1) the relationship between H_{93} and $\Delta W/W$ can be plotted and the result compared with fast diamagnetic loop data as shown in figure 4.2.2. If correct, this model suggests that there is an inescapable link between ELM amplitude and the pedestal contribution to the global energy confinement in discharges where impurity seeding is used to drive up the radiative losses and reduce the severity of the ELMs.
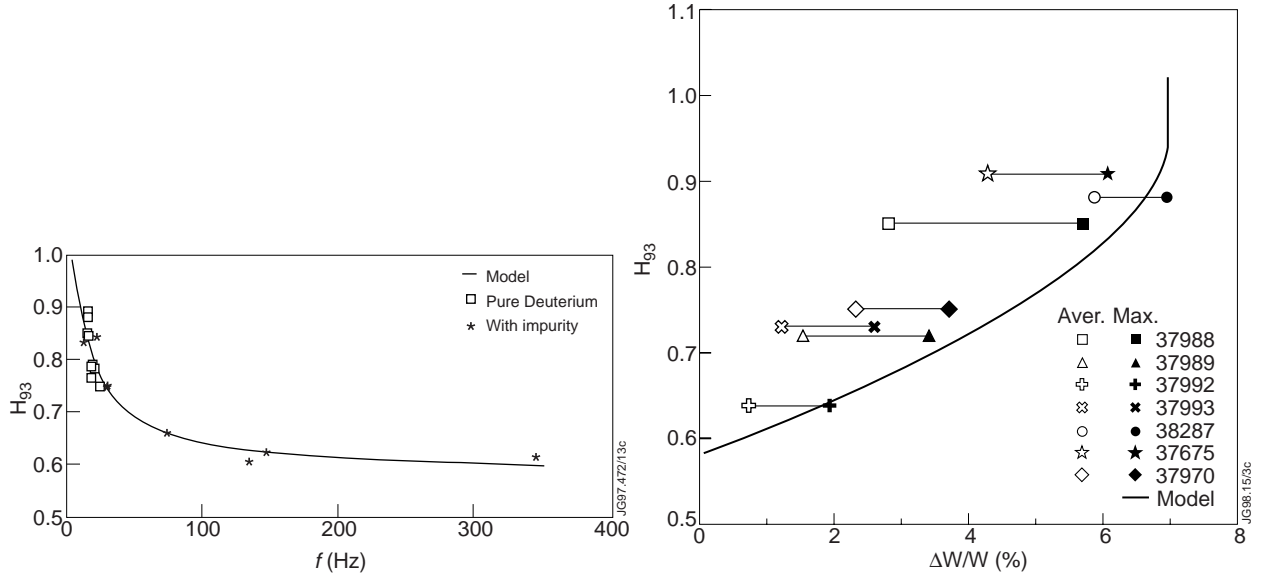

Figure 4.2.1 H93 vs ELM frequency from experiment and model. Experimentally the only variables are the impurity and deuterium fuelling rates.

Figure 4.2.2 H_{93} vs normalised ELM energy $\Delta W/W$ from experiment and model from the same group of pulses as are shown in the previous figure. Both the average and maximum $\Delta W/W$ are indicated.

Whilst the arguments presented in this section allow one to keep very different seeded and unseeded discharges within the same scaling law it still leaves open the question as to why the global confinement scaling in the radiative ρ^* pulses of figure 3.3.1 does not reflect the Gyro-Bohm like scaling of the core χ_{eff}. Although the value of ft_E varied over the ρ^* scan from 4.2 (1MA/1T) up to 16 (2.6MA/2.6T) equation 4.2.1 would predict that the effect was almost saturated. Unfortunately limitations of the edge ECE system mean that the actual pedestal height cannot be measured but the model predicts that the changes ft_E can at most account for 5% departure of the stored energy from ITERH93-P scaling. To reconcile the global and local confinement scalings 30% difference in stored energy must be accounted for. Another 10% of this can be attributed to the fact that the power deposition profile for the neutral beams is more peaked at 1MA/1T. The remaining 15% appears to be related to the more Bohm like scaling near the plasma edge which is not well resolved by the TRANSP analysis due to the limitations of the diagnostic data.

5. DISCUSSION

5.1 Implications for ITER

Seeded radiating discharges in JET have achieved a level of fractional radiated losses which, coupled with small high frequency ELMs, appear to offer a solution to the heat load problem in the ITER divertor. Although the incremental Z_{eff} is very high in these discharges, when scaled to ITER the impurity levels are within a factor two of the acceptable value due to the large main plasma surface area and high density required in ITER. The slight hollowness of the Z_{eff} profiles seen in JET, if applicable to ITER, may also help bridge the gap. Although this prediction is still marginal for ITER, the favourable conclusion is that the ITER requirement lies within the scatter of the experimental data and hence does not require any dramatic improvement in divertor performance. This is a fortunate result since the concept of a divertor with strong retention of impurities and high fractional radiated powers from within the divertor volume has not yet been realised. However these results do raise the question as to whether the large volume devoted to the deep divertor in ITER is justifiable if most of the losses are outside the divertor or in the vicinity of the X-point. In favour of the deep divertor is evidence that closing the JET divertor has raised the divertor neutral losses while at the same time this does not appear to have significantly altered the density limit. Also, closing the divertor has raised the divertor neutral pressure and so increased the particle removal rate [*Horton*]. Core helium concentrations in ITER are expected to be determined by the exhaust rate at the divertor. A reduced concentration of helium in the core would allow a higher concentration of seeded impurities to be tolerated so there is an indirect benefit from improved divertor closure.

A difficult issue for the radiative regime in ITER is prediction of the energy confinement time. The error bars on the projections for type I ELMy H-mode confinement are already marginal for an adequate prediction for the ITER ignition margin but sufficient accuracy now seems within grasp through the adoption of the ρ_* scaling dimensionless variable approach [*Cordey*]. Unfortunately, extending this methodology to high density radiative discharges, where ITER actually needs to operate, appears to be impossible when dealing with global definitions of the dimensionless variables since the requirements for high radiative losses over constrains the other variables. However, the experiments carried out at JET in which Z_{eff}, β, q_{95}, f_{rad} and plasma shape were kept constant appears to be the best compromise. Even so, various factors mean that the global confinement scaling in the radiative regime is closest to Bohm. Fortunately, the energy confinement scaling in the core appears Gyro-Bohm like. However, the edge region is important for ITER and current analysis suggests a less favourable scaling for this part of the plasma. Diagnostic limitations mean that a detailed analysis of this region is not possible.

The decrease in energy confinement time from unseeded to highly radiative regimes is dominated by the impact of the radiating layer on the edge. This appears to make sense in terms of edge operational space if one considers how the averaged pedestal pressure varies with ELM

frequency. What this implies for ITER is still an open question because it depends on a knowledge of exactly how the pedestal height and the ELM trajectories scale. This effect also tends to mask the intrinsic question of how the core confinement scales. The local transport analysis of radiative discharges carried out at JET supports the idea that the core confinement retains a Gyro-Bohm like scaling with ρ_* although the uncertainties are large. Consideration of the pressure cycles during ELMs suggests that there is an inextricable link between the pedestal height and the drop in stored energy associated with the ELMs. As a result, although the core confinement scaling seems favourable, ITER may not be able to rely on a large additional contribution from the edge pedestal since this may result in ELMs whose transient power loads cannot be handled by the divertor [*Gauthier*]. Figure 4.2.2 illustrates another potential problem for ITER in that although it possible to drive the average *ΔW/W* per ELM below the 1% level the ELM size is not uniform and there are still 2% ELMs present. The point, at which the upper limit of ELM size crosses the surface sublimation threshold is critical for ITER.

The relatively low density achieved with respect to the Greenwald Density Limit is perhaps the most serious cause for concern over the viability of highly radiative plasmas in ITER. A similar problem exists with non seeded type I ELMy H-modes. However, the apparent link between detachment and the density limit in the JET radiative discharges suggests that the detachment model for the H-mode density limit proposed by Borrass[*Borrass*] may be applicable in this case. This model is more optimistic when extrapolated to ITER than the Greenwald scaling.

6.2 Design of future experiments

Future experiments at JET will be aimed at extending the range of the radiative ρ_* experiments and to make finer steps. The relationship between confinement and $f\tau_E$ expressed in equation 4.2.1 suggests that this may be a more relevant dimensionless constraint than f_{rad} which might make the global confinement scaling more meaningful. On the practical side $f\tau_E$ is a parameter which is readily controlled. The argument that can be made against using $f\tau_E$ is that we cannot predict what the ELM frequency will be in ITER. However, since there is an upper limit on the value of *ΔW/W* which the ITER divertor can tolerate, equation 4.2.2 can be used to define a minimum acceptable ELM frequency since the two quantities would appear to be inextricably linked. If this minimum ELM frequency is not achieved as a natural consequence of the ITER operating regime then means will have to found to impose it by gas or impurity fuelling or by other means. Hence, it may not be essential to predict the natural ELM frequency in ITER.

In parallel with this detailed study of the core, emphasis will be given to measurements of the edge pedestal using the improved diagnostics which should be available. The scaling of the stability boundaries within this diagram and the location of radiative regimes with respect to these boundaries is clearly critical for making predictions for ITER.

6 CONCLUSIONS

The current ITER design requires high radiated power fractions and small ELMs in a geometrically closed divertor. JET experiments over the last 5 years have explored this regime of impurity seeded discharges with high radiated power fractions in a series of 4 distinct divertor phases. Scalings suggest that a price will be paid for the radiative regime in terms of enhanced impurity content and reduced energy confinement but that ITER's minimum requirements could be met. The uncertainties are however still large and more detailed studies of core and pedestal scalings are required.

Doubt remains regarding the density limit which in radiative regimes lies below the Greenwald density limit. However, in this respect the radiative discharges are not significantly different from unseeded type I ELMy discharges with gas fuelling. The issue in both cases is whether the expression for the Greenwald density limit provides an accurate scaling to ITER. In contrast with conventional type I ELMy discharges, the density limit in radiative discharges appears to be associated with divertor detachment.

REFERENCES

Allen S.L .et al., Plasma Phys. Control. Fusion 37 (1995) A191-A202

Asakura N., Shimizu K., Shirai H., Koide Y., Takizuka T., Plasma Phys. Contro. Fusion 39 (1997) 1295-1314

Altmann H. and Andrew, P. "Closure of the bypass leakage around the JET divertor with polymer seals, Technical report, JET Joint Undertaking 1997, JET-P(97)42

Borrass K., Lingertat J. and Schneider R., Contrib. Plasma Phys. 38 (1998) 130

Chankin A.V. and Matthews G.F. Europhysics Conference Abstracts, Vol. 21A Part III (1997) 1009

Clement S., Campbell D.J., Chankin A.V., Coad P. et al., Europhysics Conference Abstracts, Vol. 19C Part III (1995) 309

Connor J.W. and Taylor J.B, Nuclear Fusion 17 (1977) 1047

Cordey J.G., presented on behalf of the ITER Confinement and Modelling Working Group, Plasma Phys. Control. Fusion, 39 (1997) B115-B127

Ehrenberg J.K., Campbell D.J., Harbour P.J., Horton L.D., et al., J. Nucl. Mater. 241-243 (1997) 420

Erents S.K., LaBombard B., Chankin A.V., Davies S.J., et al., Europhysics Conference Abstracts, Vol. 21A Part I (1997) 121

Fishpool G., "Loss of Confinement Due to Reduction of the Edge Pedestal in JET", submitted for publication in Nuclear Fusion, JET preprint JET-P(97)30

Gauthier E., Chankin A., Clement S., Coad P. et al., Europhysics Conference Abstracts, Vol. 21A Part I (1997) 61

Greenwald M., et al., Nuc. Fus., 28 (1988) 2199

Gruber O., Mertens V., Neuhauser J., Ryter F., Suttrop W. et al. Plasma Phy. Control. Fusion 39(1997) B19-B38

Horton L.D. et al., "Studies in JET Divertors of Varied Geometry I: Non Seeded Operation" companion paper submitted for publication in Nuclear Fusion (1998)

ITER H-Mode Database Working Group, Nucl. Fusion 34 (1994) 131

Ingesson L.C., et al., Europhysics Conference Abstracts, Vol. 21A Part I (1997) 113

Itami K.and the JT60 Team, Plasma Phys. Control. Fusion 37 (1995) A255-A265

Janeschitz G., Pacher H.D., Federici G. et al., 16th IAEA Fusion Energy Conf, Montreal, IAEA-CN-64/F-2 (1996)

Kallenbach A., Dux R., Mertens V., Gruber O. et al., Nuclear Fusion, Vol. 35, No. 10 (1995) 1231-1246

Keilhacker M. for the JET Team, Plasma Phys. Control. Fusion 39 (1997) B6-B7

Kotschenreuter M. et al., IAEA-CN-64/D1-5, Montreal, 1996

Lackner K., Comments on Plasma Physics and Controlled Fusion 15 (1994) 359

Lingertat J., 4th European Fusion Physics Workshop, Sollentuna Sweden (1996)

Lipschultz B., Goetz J.A., LaBombard B., McCracken G.M., et al., J. Nucl. Mater. 241-243 (1997) 771-776

Loarte A., Monk R.D., Martin-Solis J.R., Campbell D.J. et al., Nuclear Fusion, 38 (1998) 331

Loarte A., J. Nucl. Mater. 241-243 (1997b) 118

McCracken G. Stamp M.F., Monk R.D., Meigs A. et al. submitted to Nuclear Fusion, JET preprint JET-P(97)44

McCracken G. et al., companion paper submitted to Nuclear Fusion "Studies in JET Divertors of Varied Geometry III: Intrinsic Impurity Behaviour" (1998)

Matthews G.F., et al., J. Nucl. Mater. 220-222 (1995a) 104-116

Matthews G.F. for the JET Team, Plasma Phys. Control. Fusion 37 (1995b) A227-A239

Matthews G.F., Allen S., Asakura N., Goetz J., et al., J. Nucl. Mater. 241-243 (1997) 450-455

Matthews G.F., Balet B., Cordey J.G., Fishpool G.,, et al., Europhysics Conference Abstracts, Vol. 21A Part III (1997b) 1045

Maggi C.F., Elder J.D., Fundamenski W., Giannella R., et al., J. Nucl. Mater. 241-243 (1997) 414-419

Monk R.D., A.Loarte, A.Chankin, S.Clement et al. Contrib. Plasma Phys. 36(1996) S, 37-44

Neuhauser J. et al., Plasma Phys. Control. Fusion 37 (1995) A37-A51

C.C.Petty, T.C.Luce, Nuc. Fus. Vol. 37, No. 1 (1997)

S.Putvinski, R.Aymar, D.Boucher, C.Z.Cheng, et al.,Proceedings of the 16th Int. Conf. on Fusion Energy Montrea,l IAEA-CN-64/F-1, Vol. II (1996) 737

Reichle R. et al. Europhysics Conference Abstracts, Vol. 19C Part III (1995) 85

Reichle R. et al., J. Nucl. Mater. 241-243 (1997) 456

Righi E., Bartlett D., Conway G.D., Cordey J.G. et al., Europhysics Conference Abstracts, Vol. 21A Part I (1997) 93

Samm U. et al., Plasma Phys. Cont. Fus. 35 (1993) B167-175

Schneider R., Coster D.P., Neuhauser J., Bosch S., et al., Europhysics Conference Abstracts, Vol. 19C Part IV (1995) 285

Stangeby P.C., Elder J.D., Fundamenski W., Loarte A., et al., J. Nucl. Mater, 241-243(1997) 358

Stork D. for the JET Team, IAEA-CN-64/A1-1, Montreal, Vol.1 (1996) 189

Taroni A., et al., J. Nucl. Mater., 220-222(1995) 1086

Vlases G.. for the JET Team, IAEA-CN-64/A4-1, Montreal, Vol. I (1996) 371

Vlases G., Janeschitz G., Matthews G.F., et al., J. Nucl. Mater., 196-198 (1992) 392-397

Wilson H.R. and Connor J.W., Europhysics Conference Abstracts, Vol. 21A Part I (1997) 289

Yushmanov P.N., et al., Nucl. Fusion 30 (1990) 1999